

FAST STANDING MODES IN TRANSVERSELY NONUNIFORM SOLAR CORONAL SLABS: EFFECTS OF A FINITE PLASMA BETA

Shao-Xia Chen¹

Bo Li¹

bbl@sdu.edu.cn

Sanjay Kumar¹

Hui Yu¹

and

Mijie Shi¹

ABSTRACT

We examine the dispersive properties of linear fast standing modes in transversely nonuniform solar coronal slabs with finite gas pressure, or, equivalently, finite plasma beta. We derive a generic dispersion relation governing fast waves in coronal slabs for which the continuous transverse distributions of the physical parameters comprise a uniform core, a uniform external medium, and a transition layer (TL) in between. The profiles in the TL are allowed to be essentially arbitrary. Restricting ourselves to the first several branches of fast modes, which are of most interest from the observational standpoint, we find that a finite plasma beta plays an at most marginal role in influencing the periods (P), damping times (τ), and critical longitudinal wavenumbers (k_c), when both P and τ are measured in units of the transverse fast time. However, these parameters are in general significantly affected by how the TL profiles are described. We conclude that, for typical coronal structures, the dispersive properties of the first several branches of fast standing modes can be evaluated with the much simpler theory for cold slabs provided that the transverse profiles are properly addressed and the transverse Alfvén time in cold MHD is replaced with the transverse fast time.

¹Shandong Provincial Key Laboratory of Optical Astronomy and Solar-Terrestrial Environment, Institute of Space Sciences, Shandong University, Weihai 264209, China

Subject headings: magnetohydrodynamics (MHD) — Sun: corona — Sun: magnetic fields — waves

1. INTRODUCTION

The past two decades have seen rapid development of solar magneto-seismology (SMS) in general, and coronal seismology in particular. On the one hand, this was made possible by the abundant measurements of low-frequency waves and oscillations in the Sun’s atmosphere (see, e.g., [Banerjee et al. 2007](#); [De Moortel & Nakariakov 2012](#); [Wang 2016](#), for recent reviews). On the other hand, an increasingly refined theoretical understanding has become available regarding the collective wave modes in magnetized plasma inhomogeneities (see, e.g., [Roberts 2000](#); [Nakariakov & Verwichte 2005](#); [Roberts 2008](#); [Nakariakov et al. 2016](#)). For this latter purpose, plasma inhomogeneities are traditionally seen as field-aligned magnetic cylinders, following the seminal studies by e.g., [Rosenberg 1970](#), [Zajtsev & Stepanov 1975](#), [Spruit 1982](#), [Edwin & Roberts 1983](#), and [Cally 1986](#). In fact, the modern terminology in SMS has largely come from this series of studies, allowing one to distinguish between body and surface modes or leaky and trapped modes (see, e.g., [Nakariakov & Verwichte 2005](#)). Among the infinitely many modes that a plasma cylinder can host, kink (with azimuthal wavenumber $m = 1$) and sausage ($m = 0$) modes have received most attention. This is understandable given that kink modes are the only ones that displace the cylinder axis and therefore may naturally account for the extensively measured transverse displacements of magnetic flux tubes in both the corona (e.g., [Aschwanden et al. 1999](#); [Nakariakov et al. 1999](#); [Ofman & Wang 2008](#); [Erdélyi & Taroyan 2008](#); [Verwichte et al. 2009](#); [Aschwanden & Schrijver 2011](#)) and the chromosphere (e.g., [Morton et al. 2012](#); [Kuridze et al. 2013](#); [Jafarzadeh et al. 2017](#); [Mooroogen et al. 2017](#)). On the other hand, sausage modes in flare loops have been invoked to account for a significant fraction of quasi-periodic pulsations in solar flare light curves (see, e.g., [Nakariakov & Melnikov 2009](#); [Van Doorselaere et al. 2016](#), for recent reviews). There have also been a substantial number of pieces of observational evidence showing the existence of sausage modes in magnetic pores (e.g., [Dorotovič et al. 2008](#); [Morton et al. 2011](#); [Dorotovič et al. 2014](#); [Grant et al. 2015](#); [Freij et al. 2016](#)) and coronal loops (e.g., [Su et al. 2012](#); [Tian et al. 2016](#); [Dennis et al. 2017](#)).

Wave-guiding plasma inhomogeneities in the solar atmosphere have also been extensively modeled as magnetic slabs (e.g., [Edwin & Roberts 1982](#); [Murawski & Roberts 1993](#); [Ofman et al. 1994](#); [Porter et al. 1994](#); [Huang et al. 1999](#); [Terradas et al. 2005](#); [Li et al. 2013](#); [Chen et al. 2014](#); [Hornsey et al. 2014](#); [Yu et al. 2015, 2016b](#); [Allcock & Erdélyi 2017](#)). This practice can be justified given that a slab rather than a cylindrical geometry is more suit-

able for interpreting a considerable number of observations. For instance, Sunward moving tadpole-like structures in post-flare supra-arcades as observed by the Transition Region And Coronal Explorer (TRACE) were attributed to fast kink waves in vertical slab-like structures (Verwichte et al. 2005). The extensively measured prominence oscillations were also interpreted in terms of collective modes in dense slabs embedded in the corona (see Arregui et al. 2012, and references therein). Interestingly, the theoretical results on collective modes in wave-guiding slabs also apply even when current sheets are embedded, albeit in the limit of vanishing resistivity (e.g., Edwin et al. 1986; Smith et al. 1997; Feng et al. 2011). It is then no surprise to see that fast kink waves in magnetic slabs were invoked to account for the large-scale propagating disturbances in current sheets above streamer helmets, as imaged with the Large Angle and Spectrometric Coronagraph (LASCO) on board the Solar and Heliospheric Observatory satellite (SOHO) (Chen et al. 2010, 2011). Furthermore, fast sausage modes guided by flare current sheets were employed to interpret some fine structures in broadband type IV radio bursts (e.g., Jelínek & Karlický 2012; Karlický et al. 2013; Yu et al. 2016b).

For mathematical simplicity, analytical studies of fast modes in magnetic slabs usually adopt either one or both of the following two assumptions. One is the cold ($zero-\beta$) MHD limit, where thermal pressure is neglected. The other is that the plasma and magnetic parameters are transversely structured in a top-hat fashion. Relaxing the second assumption, some studies are available where the continuous transverse profiles are either some specific ones (e.g., Edwin & Roberts 1988; Nakariakov & Roberts 1995b; Macnamara & Roberts 2011; Lopin & Nagorny 2015) or essentially arbitrary (Yu et al. 2015, hereafter paper I). Relaxing the first assumption, available studies nonetheless tend to adopt a top-hat profile for the transverse distributions of physical parameters (e.g., Edwin & Roberts 1982; Inglis et al. 2009). In cylindrical geometry, we have offered an analytical study on fast sausage modes in coronal tubes for which the gas pressure is finite and the transverse profiles are essentially arbitrary (Chen et al. 2016, hereafter paper II). The aim of the present manuscript is to offer a slab counterpart of our paper II.

Before proceeding, a few words seem necessary to justify the motivation of this study. First, such parameters as temperature, density, and the magnetic field strength are evidently more likely to be continuously distributed across magnetic structures. Second, the plasma β , which measures the importance of the gas pressure relative to the magnetic one, is not necessarily small but may reach a value of order unity in hot and dense solar structures (e.g., Melnikov et al. 2005; Wang et al. 2007). Third, while the combined effects of continuous transverse profiles and finite gas pressure can be readily addressed by numerical simulations (e.g., Inglis et al. 2009; Jelínek & Karlický 2012; Yu et al. 2016b), performing a largely analytical eigen-mode analysis for fast collective modes still proves useful. On the one hand,

examining the dispersive properties is much less numerically expensive. On the other hand, the frequency-dependence of the axial group speed can be readily computed, which will facilitate the interpretation of the numerical results on impulsively generated wave trains in, say, flare current sheets (Jelínek et al. 2012; Karlický et al. 2013; Mészárosová et al. 2014). The applications in this regard have been offered in Yu et al. (2016a) and Yu et al. (2017).

This manuscript is structured as follows. Section 2 presents the necessary description for an equilibrium straight magnetic slab. In Section 3, we derive a generic dispersion relation (DR) for linear magneto-acoustic waves in magnetic slabs with nonnegligible gas pressure and rather arbitrary transverse distributions. We examine, in Section 4, the effects of a finite β on the dispersive properties of standing fast modes in substantial detail. Section 5 closes this manuscript with our summary and some concluding remarks.

2. DESCRIPTION FOR THE EQUILIBRIUM SLAB

2.1. Overall Description

We model coronal structures as straight, gravity-free, density-enhanced slabs with mean half-width R . We adopt a Cartesian coordinate system (x, y, z) , where the z -axis coincides with the axis of the slab. The equilibrium magnetic field \mathbf{B} is in the z -direction and is a function of x only. We further assume that both plasma density ρ and temperature T depend only on x . Note that we are allowed to prescribe the x -dependence of only two parameters in $[B, \rho, T]$, since they are related by the transverse force balance condition

$$p(x) + \frac{B^2(x)}{8\pi} = \text{const} \equiv \alpha, \quad (1)$$

in which the gas pressure p is given by

$$p = \frac{2k_{\text{B}}}{m_p} \rho T. \quad (2)$$

Here k_{B} is the Boltzmann constant and m_p the proton mass.

The following characteristic speeds are necessary for us to proceed. The adiabatic sound and Alfvén speeds are defined as

$$c_{\text{s}}^2 = \frac{\gamma p}{\rho}, \quad \text{and} \quad v_{\text{A}}^2 = \frac{B^2}{4\pi\rho}, \quad (3)$$

where $\gamma = 5/3$ is the adiabatic index. It then follows that the plasma $\beta \equiv 8\pi p/B^2$ reads

$$\beta = \frac{2}{\gamma} \frac{c_{\text{s}}^2}{v_{\text{A}}^2}. \quad (4)$$

We then define the fast and tube speeds as

$$v_f^2 = c_s^2 + v_A^2, \quad (5)$$

and

$$c_T^2 = \frac{c_s^2 v_A^2}{c_s^2 + v_A^2}, \quad (6)$$

respectively.

2.2. Description for Transverse Profiles

We assume that the equilibrium parameters are symmetric about $x = 0$. In the half-plane $x > 0$, we choose to prescribe the equilibrium density $\rho(x)$ and temperature $T(x)$ as

$$\rho(x) = \begin{cases} \rho_i, & 0 \leq x \leq x_i = R - l/2, \\ \rho_{\text{tr}}(x) = \mathcal{F}(\rho_i, \rho_e; x), & x_i \leq x \leq x_e = R + l/2, \\ \rho_e, & x \geq x_e, \end{cases} \quad (7)$$

and

$$T(x) = \begin{cases} T_i, & 0 \leq x \leq x_i, \\ T_{\text{tr}}(x) = \mathcal{G}(T_i, T_e; x), & x_i \leq x \leq x_e, \\ T_e, & x \geq x_e. \end{cases} \quad (8)$$

This sandwich-like profile means that the equilibrium configuration comprises a uniform core (denoted by subscript i), a uniform external medium (subscript e), and a transition layer (TL) connecting the two. This TL is of width l and centered around the mean half-width R . Furthermore, $\mathcal{F}(\rho_i, \rho_e; x)$ and $\mathcal{G}(T_i, T_e; x)$ are functions that continuously vary from the core-TL interface ($x = x_i$) to the TL-external-medium interface ($x = x_e$). In addition, we require that the functions \mathcal{F} and \mathcal{G} are smooth at $x = R$, making it possible to Taylor expand $\rho_{\text{tr}}(x)$ and $T_{\text{tr}}(x)$ around $x = R$. The result is

$$\rho_{\text{tr}}(\epsilon) = \sum_{n=0}^{\infty} \rho_n \epsilon^n, \quad T_{\text{tr}}(\epsilon) = \sum_{n=0}^{\infty} T_n \epsilon^n, \quad (9)$$

where $\epsilon \equiv x - R$, $\rho_0 = \rho|_{\epsilon=0}$, $T_0 = T|_{\epsilon=0}$ and

$$\rho_n = \frac{1}{n!} \left. \frac{d^n \rho(\epsilon)}{d\epsilon^n} \right|_{\epsilon=0}, \quad T_n = \frac{1}{n!} \left. \frac{d^n T(\epsilon)}{d\epsilon^n} \right|_{\epsilon=0}, \quad n \geq 1. \quad (10)$$

In the TL, we Taylor-expand the characteristic speeds c_s^2 and v_A^2 as

$$c_s^2 = \sum_{n=0}^{\infty} C_n \epsilon^n, \quad v_A^2 = \sum_{n=0}^{\infty} V_n \epsilon^n,$$

where

$$C_n = \frac{2\gamma k_B T_n}{m_p}, \quad (11)$$

and

$$\begin{cases} V_0 = \frac{2\alpha}{\rho_0} - \frac{2}{\gamma} C_0, \\ V_n = -\frac{1}{\rho_0} \left(\frac{2}{\gamma} \sum_{l=0}^n C_l \rho_{n-l} + \sum_{l=0}^{n-1} V_l \rho_{n-l} \right), \quad n \geq 1. \end{cases} \quad (12)$$

Note that the force balance condition (Eq. 1) has been used to derive the coefficients V_n .

3. DISPERSION RELATIONS OF FAST WAVES

3.1. Dispersion Relations for Arbitrary Transverse Profiles in the TL

Now we examine linear fast waves, by which we mean waves with phase speeds always exceeding c_s , in magnetic slabs pertaining to the configuration that was just described. For this purpose we adopt the framework of ideal MHD. Let $\delta\rho$, $\delta\mathbf{v}$, $\delta\mathbf{B}$, and δp denote the perturbations to the density, velocity, magnetic field and pressure, respectively. We consider only fast waves in the $x-z$ plane by letting $\partial/\partial y \equiv 0$, and $\delta B_y = \delta v_y = 0$. Any perturbation $\delta f(x, z; t)$ can be Fourier-decomposed as

$$\delta f(x, z; t) = \text{Re} \left\{ \tilde{f}(x) \exp[-i(\omega t - kz)] \right\}. \quad (13)$$

Now with the definition of the Fourier amplitude for the Lagrangian displacement $\tilde{\xi}_x = i\tilde{v}_x/\omega$, it is straightforward to show that $\tilde{\xi}_x$ is governed by

$$\frac{d}{dx} \left[\frac{\rho(c_s^2 + v_A^2)(\omega^2 - k^2 c_T^2)}{\omega^2 - k^2 c_s^2} \frac{d\tilde{\xi}_x}{dx} \right] + \rho(\omega^2 - k^2 v_A^2) \tilde{\xi}_x = 0. \quad (14)$$

The solution to Equation (14) in a uniform medium is well-known (e.g., [Edwin & Roberts 1982](#)). With coronal applications in mind, we assume that the ordering $v_{Ae} > v_{Ai} > c_{si} > c_{se}$ holds and $c_s < v_A$ in the TL. In this case, Equation (14) is singularity-free for fast waves. This is because fast modes always propagate faster than the tube speed, and hence cannot couple to the slow continuum. Furthermore, when propagating strictly in the $x-z$ plane, they

are not resonantly coupled to the shear Alfvén continuum either (e.g., [Arregui et al. 2007b](#)). The solution to Equation (14) in the TL can then be expressed as linear combinations of two linearly independent solutions, $\tilde{\xi}_{\text{tr},1}$ and $\tilde{\xi}_{\text{tr},2}$,

$$\tilde{\xi}_{\text{tr},1}(\epsilon) = \sum_{n=0}^{\infty} a_n \epsilon^n, \quad \tilde{\xi}_{\text{tr},2}(\epsilon) = \sum_{n=0}^{\infty} b_n \epsilon^n. \quad (15)$$

Now the standard practice will be to insert the regular series expansion (15) into Equation (14) such that the recurrence relations for the coefficients a_n and b_n can be found. For this purpose, however, it turns out to be more convenient to work with an equation where ρ is not directly present. Given the force balance condition (1), it is straightforward to show that ρ can be expressed as

$$\rho = \frac{2\alpha}{v_{\text{A}}^2 + 2c_{\text{s}}^2/\gamma}.$$

As a result, Equation (14) can be reformulated into

$$\frac{d}{dx} \left[\frac{(c_{\text{s}}^2 + v_{\text{A}}^2)(\omega^2 - k^2 c_{\text{T}}^2)}{(2c_{\text{s}}^2 + \gamma v_{\text{A}}^2)(\omega^2 - k^2 c_{\text{s}}^2)} \frac{d\tilde{\xi}_x}{dx} \right] + \frac{\omega^2 - k^2 v_{\text{A}}^2}{2c_{\text{s}}^2 + \gamma v_{\text{A}}^2} \tilde{\xi}_x = 0. \quad (16)$$

Then the recurrence relations can be found by inserting the expansion (15) into Equation (16) and demanding the coefficient of ϵ^n ($n = 0, 1, 2, \dots$) to be zero. Without loss of generality, we choose

$$a_0 = R, \quad a_1 = 0, \quad \text{and} \quad b_0 = 0, \quad b_1 = 1. \quad (17)$$

The expressions for the rest of the coefficients are too lengthy and therefore are given in Appendix A.1. It suffices to note that they involve only the coefficients C_n and V_n . All in all, $\tilde{\xi}_x(x)$ can be expressed as

$$\tilde{\xi}_x(x) = \begin{cases} \begin{cases} A_i \sin(\mu_i x) & \text{sausage} \\ A_i \cos(\mu_i x) & \text{kink} \end{cases}, & 0 \leq x \leq x_i, \\ A_1 \tilde{\xi}_{\text{tr},1}(\epsilon) + A_2 \tilde{\xi}_{\text{tr},2}(\epsilon), & x_i \leq x \leq x_e, \\ A_e \exp(i\mu_e x), & x \geq x_e, \end{cases} \quad (18)$$

where A_i , A_e , A_1 and A_2 are arbitrary constants. In addition,

$$\mu_{i,e}^2 = \frac{(\omega^2 - k^2 v_{\text{Ai},e}^2)(\omega^2 - k^2 c_{\text{si},e}^2)}{(c_{\text{si},e}^2 + v_{\text{Ai},e}^2)(\omega^2 - k^2 c_{\text{Ti},e}^2)}. \quad (19)$$

To derive the DR, one also requires the explicit expressions for the Fourier amplitude of the Eulerian perturbation of total pressure \tilde{p}_{T} . It is related to the Lagrangian displacement

via (e.g., [Edwin & Roberts 1982](#))

$$\tilde{p}_T = -\frac{\rho(c_s^2 + v_A^2)(\omega^2 - k^2 c_T^2)}{\omega^2 - k^2 c_s^2} \tilde{\xi}'_x, \quad (20)$$

where the prime $' = d/dx$. With the aid of Equation (18), one finds that

$$\tilde{p}_T(x) = \begin{cases} -A_i \mu_i \frac{\rho_i(c_{si}^2 + v_{Ai}^2)(\omega^2 - k^2 c_{Ti}^2)}{\omega^2 - k^2 c_{si}^2} \begin{cases} \cos(\mu_i x) & \text{sausage} \\ -\sin(\mu_i x) & \text{kink} \end{cases}, & 0 \leq x \leq x_i, \\ -i A_e \mu_e \exp(i \mu_e x) \frac{\rho_e(c_{se}^2 + v_{Ae}^2)(\omega^2 - k^2 c_{Te}^2)}{\omega^2 - k^2 c_{se}^2}, & x \geq x_e, \end{cases}$$

in the uniform core and external medium. In the TL it is given by

$$\tilde{p}_T(\epsilon) = -\frac{\sum_{l=0}^{\infty} \rho_l \epsilon^l \left(\omega^2 \sum_{n=0}^{\infty} C_n \epsilon^n + \omega^2 \sum_{n=0}^{\infty} V_n \epsilon^n - k^2 \sum_{n=0}^{\infty} C_n \epsilon^n \sum_{j=0}^{\infty} V_j \epsilon^j \right)}{\omega^2 - k^2 \sum_{n=0}^{\infty} C_n \epsilon^n} \left[A_1 \tilde{\xi}'_{\text{tr},1}(\epsilon) + A_2 \tilde{\xi}'_{\text{tr},2}(\epsilon) \right]. \quad (21)$$

Requiring that $\tilde{\xi}_x$ and \tilde{p}_T be continuous at $x = x_i$ and $x = x_e$ yields four algebraic equations governing $[A_1, A_2, A_i, A_e]$. For these solutions to be non-trivial, one finds that

$$\frac{X_i \tilde{\xi}'_{\text{tr},1}(\epsilon_i) + \Lambda_i \tilde{\xi}'_{\text{tr},1}(\epsilon_i)}{X_i \tilde{\xi}'_{\text{tr},2}(\epsilon_i) + \Lambda_i \tilde{\xi}'_{\text{tr},2}(\epsilon_i)} - \frac{X_e \tilde{\xi}'_{\text{tr},1}(\epsilon_e) + \Lambda_e \tilde{\xi}'_{\text{tr},1}(\epsilon_e)}{X_e \tilde{\xi}'_{\text{tr},2}(\epsilon_e) + \Lambda_e \tilde{\xi}'_{\text{tr},2}(\epsilon_e)} = 0, \quad (22)$$

in which $\epsilon_{i,e} = \mp l/2$ and

$$\Lambda_{i,e} = -\frac{\sum_{l=0}^{\infty} \rho_l \epsilon_{i,e}^l \left(\omega^2 \sum_{n=0}^{\infty} C_n \epsilon_{i,e}^n + \omega^2 \sum_{n=0}^{\infty} V_n \epsilon_{i,e}^n - k^2 \sum_{n=0}^{\infty} C_n \epsilon_{i,e}^n \sum_{j=0}^{\infty} V_j \epsilon_{i,e}^j \right)}{\omega^2 - k^2 \sum_{n=0}^{\infty} C_n \epsilon_{i,e}^n}, \quad (23)$$

$$X_i = \frac{\rho_i (\omega^2 - k^2 v_{Ai}^2)}{\mu_i} \times \begin{cases} \cot(\mu_i x_i) & \text{sausage} \\ -\tan(\mu_i x_i) & \text{kink} \end{cases}, \quad X_e = \frac{i \rho_e (\omega^2 - k^2 v_{Ae}^2)}{\mu_e}.$$

Equation (22) is the DR we are looking for, and is valid for rather arbitrary choices of the transverse profiles in the TL.

3.2. Dispersion Relation for Top-hat Transverse Profiles

For future reference, this section examines what happens for top-hat profiles by letting $l/R \rightarrow 0$ in the DR (22). To do this we retain only terms to the zeroth order in l/R . Hence

$x_i \approx x_e \approx R$ and $\epsilon_i \approx \epsilon_e \approx 0$. Now that $\Lambda_i \approx \Lambda_e$, it follows from Equation (22) that

$$(X_i - X_e)(a_1 b_0 - a_0 b_1) = 0. \quad (24)$$

The term $a_1 b_0 - a_0 b_1$ is not allowed to be zero because $\tilde{\xi}_{\text{tr},1}(\epsilon)$ and $\tilde{\xi}_{\text{tr},2}(\epsilon)$ are linearly independent. As a result, $X_i = X_e$. Recalling the definitions for X_i and X_e as given in Equation (23), the DR in this limit simplifies to the well-known form (e.g., [Edwin & Roberts 1982](#))

$$\frac{i\rho_e(\omega^2 - k^2 v_{\text{Ae}}^2)}{\mu_e} = \frac{\rho_i(\omega^2 - k^2 v_{\text{Ai}}^2)}{\mu_i} \times \begin{cases} \cot(\mu_i R) & \text{sausage} \\ -\tan(\mu_i R) & \text{kink} \end{cases}. \quad (25)$$

For kink and sausage modes alike, there are infinitely many branches of solutions to Equation (25), with the n -th ($n = 1, 2, 3, \dots$) branch characterized by the appearance of $n - 1$ permanent transverse nodes for $\tilde{\xi}_x$ in the interval $0 < x < \infty$. Except for the first kink branch, there always exists a critical wavenumber k_c below which fast waves are no longer trapped. This k_c can be expressed as (e.g., [Nakariakov & Roberts 1995a](#); [Li et al. 2013](#))

$$k_c R = g_n \sqrt{\frac{(c_{\text{si}}^2 + v_{\text{Ai}}^2)(v_{\text{Ae}}^2 - c_{\text{Ti}}^2)}{(v_{\text{Ae}}^2 - c_{\text{si}}^2)(v_{\text{Ae}}^2 - v_{\text{Ai}}^2)}} \quad (26)$$

with g_n given by

$$g_n = \begin{cases} \left(n - \frac{1}{2}\right)\pi & \text{sausage}, \\ (n - 1)\pi & \text{kink}, \end{cases} \quad (27)$$

where $n = 1, 2, 3, \dots$. In addition, one can readily derive the expressions for the angular frequencies ω for fast waves in the long-wavelength (or thin-slab) limit by letting $kR \rightarrow 0$. In this case, the angular frequency for the first kink branch approaches zero. For the rest of the fast modes, ω can be shown to have the following form

$$\begin{aligned} \omega_{\text{R}}|_{k \rightarrow 0} &= g_n \frac{v_{\text{fi}}}{R}, \\ \omega_{\text{I}}|_{k \rightarrow 0} &= -\frac{v_{\text{fi}}}{2R} \ln \frac{1 + \rho_e v_{\text{fe}} / (\rho_i v_{\text{fi}})}{1 - \rho_e v_{\text{fe}} / (\rho_i v_{\text{fi}})}, \end{aligned} \quad (28)$$

where $v_{\text{fi},e}$ is the internal (external) fast speed. In addition, ω_{R} (ω_{I}) represents the real (imaginary) part, with the non-zero ω_{I} arising from lateral leakage. (Note that g_n is different for kink and sausage modes.) Equation (28) extends the results in [Terradas et al. \(2005\)](#) by allowing for a finite plasma beta. Two things are immediately clear. One is that the damping time associated with lateral leakage is independent of the branch label n . The other is that the angular frequency is associated with the transverse fast time R/v_{fi} . This

is understandable given that in the long-wavelength limit, the transverse spatial scale of the eigen-functions is much shorter than the longitudinal wavelength, thereby making the effective wavevector largely perpendicular to the equilibrium magnetic field. Hence the transverse fast time becomes relevant, even though, strictly speaking, the fast speed v_f as defined by Eq. (5) pertains to perpendicularly propagating fast waves in a uniform MHD medium.

4. NUMERICAL RESULTS

4.1. Prescriptions for Transition Layer Profiles and Method of Solution

Except for the assumption that $c_s(x) < v_A(x)$, no restrictions were imposed on the profiles $T(x)$ and $\rho(x)$ in the TL when the DR (22) was derived. However, the transcendental nature of the DR means that in general it needs to be solved numerically. To this end, the profiles for $T(x)$ and $\rho(x)$ should be specified. To avoid our derivation becoming unnecessarily too lengthy, we suppose that $T(x)$ and $\rho(x)$ have the same formal dependence, meaning that \mathcal{G} in Equation (8) takes the same form as \mathcal{F} in Equation (7). In addition, we will adopt a number of choices for \mathcal{F} ,

$$\mathcal{F}(\varepsilon_i, \varepsilon_e; x) = \begin{cases} \varepsilon_i - \frac{\varepsilon_i - \varepsilon_e}{l} \left(x - R + \frac{l}{2} \right), & \text{linear,} \\ \varepsilon_i - \frac{\varepsilon_i - \varepsilon_e}{l^2} \left(x - R + \frac{l}{2} \right)^2, & \text{parabolic,} \\ \varepsilon_e - \frac{\varepsilon_e - \varepsilon_i}{l^2} \left(x - R - \frac{l}{2} \right)^2, & \text{inverse - parabolic.} \end{cases} \quad (29)$$

Figure 1 uses the transverse density distribution as an example to show the different choices for $\mathcal{F}(\varepsilon_i, \varepsilon_e; x)$, where we arbitrarily choose $\rho_i/\rho_e = 50$ and $l/R = 1$.

With \mathcal{F} at hand, we can readily evaluate the coefficients C_n and V_n with Equations (11) and (12). Then with the aid of Appendix A, the coefficients a_n and b_n can be readily evaluated, making it then possible to evaluate the left-hand side (LHS) of the DR (22). Restricting us to the applications to standing fast modes in the corona, we solve the DR (22) for complex-valued angular frequencies ω at a given real-valued longitudinal wavenumber k . Similar to Paper II, we truncate the infinite series expansion in Equation (15) up to $N = 101$. To speed up the numerical computations, we also reformulate the coefficients in Appendix A.1 such that only 2-fold summations need to be evaluated (see Appendix A.2 for details). We have made sure that adopting an even larger N does not introduce any discernible difference. The end result is that, once an $\mathcal{F}(\varepsilon_i, \varepsilon_e; x)$ is chosen, the computations will yield

a dimensionless angular frequency $\omega R/v_{Ai}$ that can be formally expressed as

$$\frac{\omega R}{v_{Ai}} = \mathcal{H} \left(kR, \frac{l}{R}, \frac{\rho_i}{\rho_e}, \beta_i, \beta_e \right) \quad (30)$$

for some function \mathcal{H} , where $\beta_{i,e} = 2c_{si,e}^2/(\gamma v_{Ai,e}^2)$. Throughout this manuscript, the plasma beta in the external medium is fixed at $\beta_e = 0.01$, which is reasonable for a typical coronal environment. In addition, we will examine only fast standing modes in typical coronal structures, by which we mean that the density contrast ρ_i/ρ_e ranges from 2 to 200, and the length-to-half-width-ratio L/R ranges between 5 and 100. Note that these values are typical of flare loops and active region loops (e.g., [Aschwanden et al. 2004](#)). Note further that the longitudinal wavenumber k is related to the structure length L by $k = \pi/L$ because we shall consider only the longitudinal fundamental mode since it is the mode that is most commonly observed.

Before proceeding, let us remark that the process of deriving the DR may have introduced some spurious solutions. As suggested by e.g., [Terradas et al. \(2007\)](#) who examined fast modes in cold tubes, whether the solutions are physically relevant can be established by performing time-dependent simulations on fast modes to address whether the solutions play a role in determining the temporal evolution of the system. Similar to paper II, we have also employed PLUTO, a modular MHD code ([Mignone et al. 2007](#)), to examine both kink and sausage modes in magnetic slabs for which the equilibrium parameters are specified by Equation (29). This extensive validation study, not shown here, indicates that all the solutions to be presented are physically relevant. In addition, the values for the frequencies of fast modes derived from these time-dependent simulations are all in close agreement with what we find with the eigen-mode analysis.

4.2. Effects of a finite beta

4.2.1. Overview of Dispersion Diagrams

To lay the context for future examinations, this section provides an overview of the dispersion diagrams for various profiles in the TL. Figure 2 shows the dependence of the real (ω_R , the upper row) and imaginary (ω_I , lower) parts of the angular frequency on the longitudinal wavenumber k for kink (the left column) and sausage (right) modes. Here we choose $[l/R, \rho_i/\rho_e, \beta_i] = [1.0, 10, 1.0]$. Note that $-\omega_I$ is plotted instead of ω_I because $\omega_I \leq 0$. The results for different profiles are displayed in different colors as labeled in Figure 2(d). For comparison, the black solid curves represent the corresponding results for the top-hat profile ($l/R = 0$). In Figures 2a and 2c, the dash-dotted and dashed lines represent $\omega_R = kv_{Ae}$

and $\omega_R = kv_{Ai}$, respectively. The former separates the trapped (to its right) from the leaky (left) regime, and the latter is the lower limit that ω_R attains for fast modes. For the kink modes, we examine only the first two branches (labeled I and II in the left column), and call them “kink I” and “kink II” for brevity. Likewise, we examine only the lowest-order sausage modes, to be called “sausage I” from here onwards.

Some general features are evident from Figure 2. First, for kink and sausage modes alike, the real parts of their angular frequencies always lie above the dashed lines, meaning that these modes are always body modes. In fact, this can be said for all fast modes when $v_{Ae} > v_{Ai}$, regardless of their transverse harmonic number even though only the first several branches are shown here. Second, with the exception of kink I, all modes become leaky when k is below some critical value as evidenced by the non-zero values of ω_I in the lower panels. This is well-known for top-hat profiles (e.g., [Edwin & Roberts 1982](#)), and the numerical results shown here demonstrate that this holds for rather arbitrary choices of temperature and density profiles in the TL. Furthermore, the same behavior holds for rather arbitrary choices of the plasma beta and was seen in paper I where β was taken to be zero.

Despite the similarities in the overall behavior to the top-hat case, choosing different profiles in the TL can considerably impact the specific values of the angular frequency. Take kink II in the limit $kR \rightarrow 0$ for instance. While $[\omega_R, -\omega_I]R/v_{Ai}$ reads $[4.25, 0.464]$ for top-hat profiles (the black solid curves in Figs. 2a and 2b), it attains $[3.53, 0.473]$ ($[4.79, 0.822]$) for the profile labeled “parabolic” (“inverse-parabolic”), given by the green (blue) curves. This happens in conjunction with the rather sensitive profile dependence of the critical wavenumber k_cR . For the top-hat, parabolic and inverse-parabolic profiles, k_cR reads 0.99, 0.83, and 1.13, respectively. From an observational perspective, this means that the largely unknown transverse distribution across coronal structures can in principle be inferred by measuring such parameters as the periods and damping times of standing fast modes. In practice, this approach has been extensively employed, albeit almost exclusively based on the theoretical results found in cold MHD (e.g., [Arregui et al. 2007a](#); [Goossens et al. 2008](#); [Soler et al. 2014](#); [Guo et al. 2016](#)). Therefore what remains to be examined is how the dispersive properties of fast oscillations depend on plasma beta for a chosen profile. In what follows, we will examine how the periods ($P = 2\pi/\omega_R$), damping times ($\tau = 1/|\omega_I|$) and the critical wavenumbers (k_cR) depend on plasma beta for the profiles we chose. Fortunately, we will need only to show the results for an arbitrarily chosen profile (the parabolic one, to be specific), because the overall beta dependence remains the same for the rest of the profile choices.

4.2.2. First Branch of Fast Kink Modes

This is the simplest to examine given that kink I is always trapped (ω is always real). Figure 3 presents how ω depends on the longitudinal wavenumber kR by examining ω measured in units of both v_{Ai}/R (the left panel) and v_{fi}/R (right). Here $[l/R, \rho_i/\rho_e]$ is fixed at $[1.0, 10]$, but a number of different values for the internal plasma beta β_i are examined (see curves in different colors). From Figure 3 one sees that regardless of β_i , the angular frequency ω always increases with kR , be it normalized by the transverse fast or Alfvén time. However, Figure 3b indicates that the curves show a considerable weaker dependence on β_i than in Figure 3a. In fact, it is hard to tell the curves apart when $kR \lesssim 0.6$. This means that if we reformulate Equation (30) to

$$\frac{\omega R}{v_{\text{fi}}} = \mathcal{L} \left(kR, \frac{l}{R}, \frac{\rho_i}{\rho_e}, \beta_i, \beta_e \right), \quad (31)$$

then the function \mathcal{L} possesses a much weaker β_i dependence than \mathcal{H} , as long as the length-to-half-width-ratio $L/R \gtrsim \pi/0.6 \approx 5$. In some sense this is not surprising because Equation (28) suggests that for fast modes in infinitely thin structures, $\omega R/v_{\text{fi}}$ does not depend on β_i at all for top-hat profiles. What Figure 3 indicates is that the dependence on β_i remains weak for continuous transverse profiles provided that the coronal structures are not unrealistically thick.

Does this conclusion hold for other choices of the density contrast? We examine this by asking how much the period P may differ from its cold MHD counterpart ($\beta_i = \beta_e = 0$). To be more specific, Equation (31) suggests that P in units of R/v_{fi} at a given pair of $[\rho_i/\rho_e, L/R]$ is a function of β_i only when l/R is fixed. Let this value be denoted by $P^{\beta \neq 0}$. At the same given $[\rho_i/\rho_e, L/R]$, we then evaluate P in units of R/v_{fi} in the cold MHD limit by solving the corresponding DR (Equation 17 in Paper I). Let P^{cold} denote this value. We now define δP to be the maximal relative difference between the finite- β and cold MHD results when β_i varies between 0 and 1. In other words,

$$\delta P \equiv \max \left| \frac{P^{\beta \neq 0}(\beta_i \in [0, 1])}{P^{\text{cold}}} - 1 \right|, \quad (32)$$

which now depends on ρ_i/ρ_e and L/R only.

Figure 4 shows how δP is distributed in the $[\rho_i/\rho_e, L/R]$ space for $l/R = 1$. One sees that δP is consistently less than 10% despite the considerable variations in both ρ_i/ρ_e and L/R . Note that our cold MHD results have also shown that the periods P for fast modes pertaining to kink I do not differ much if we change one TL profile to another (paper I). In fact, for combinations of $[\rho_i/\rho_e, L/R]$ in the same range as examined here, Figure 3

in paper I demonstrates that P is rather insensitive to the dimensionless layer width l/R . It then follows that as far as kink I is concerned, one may adopt the top-hat results as a reasonable starting point when fast modes pertaining to kink I are put to seismological use. This is good news for solar MHD seismology because the top-hat results are much less complicated (compare Eq. 22 with 25). On top of that, the detailed form of the transverse distributions of the physical parameters proves difficult to infer and suffers from considerable uncertainties (e.g., Arregui & Asensio Ramos 2014; Arregui et al. 2015; Pascoe et al. 2017).

4.2.3. Second Branch of Kink Modes

The examination of the beta dependence of the dispersive properties of kink II is substantially more complicated because now the modes can become leaky for sufficiently thin structures. Figure 5 examines the influence of a finite β_i on k_c for parabolic profiles. A number of combinations $[l/R, \rho_i/\rho_e]$ are examined and given by the different colors and line styles. It is clear that the most important factor that influences $k_c R$ is the density contrast ρ_i/ρ_e . Take the green curves pertaining to $l/R = 1$ for instance. One sees that for all the β_i values examined, the critical wavenumber $k_c R$ substantially decreases when ρ_i/ρ_e increases from 10 (the solid curve) to 100 (dashed). On the other hand, examining any individual curve indicates that $k_c R$ is not sensitive to β_i , which is particularly true for large density contrasts. Even for the smaller $\rho_i/\rho_e = 10$ (the solid curves), increasing β_i leads to a decrease in k_c by no more than 5.93% for all the layer widths considered. This insensitivity to β_i of $k_c R$ can be partly understood from Equation (26), which pertains to top-hat profiles. Reformulating it to make the β_i dependence more apparent, one finds that

$$k_c R = g_2 \sqrt{-1 + \frac{\rho_{ie}^2 (1 + \beta_i)^2}{[\rho_{ie}(1 + \beta_i) - (1 + \beta_e)][\rho_{ie}(1 + \beta_i) - (\gamma\beta_i/2)(1 + \beta_e)]}} \quad (33)$$

with $g_2 = \pi$ (see Eq. 27). Here we also used the shorthand notation $\rho_{ie} = \rho_i/\rho_e$. Given that $\beta_e \ll 1$ for a typical coronal ambient, k_c can be approximated to within $\sim 10\%$ by

$$k_c R \approx g_2 \sqrt{\frac{1 + \gamma\beta_i/2}{\rho_{ie}(1 + \beta_i)}}, \quad (34)$$

when $\rho_{ie} \gtrsim 5$. Equation (34) suggests that the reason for the insensitive β_i dependence of $k_c R$ is twofold. One is the appearance of the square root, and the other is that $\gamma/2$ is close to unity. What Figure 5 suggests is that this weak dependence on β_i persists for continuous profiles.

How about the β_i dependence of the angular frequencies of kink II? We tackle this issue with the same approach as for kink I. It is just that now in addition to the periods (P), the

damping times (τ) are also relevant because these modes can be in the leaky regime. For this purpose, we also define $\delta\tau$ as

$$\delta\tau \equiv \max \left| \frac{\tau^{\beta \neq 0}(\beta_i \in [0, 1])}{\tau^{\text{cold}}} - 1 \right|, \quad (35)$$

which is identical in form to Equation (32) except that P is replaced with τ . Figure 6 then presents the distributions in the $[\rho_i/\rho_e, L/R]$ space of both δP (panel a) and $\delta\tau$ (panel b) for a dimensionless layer width $l/R = 1$. The red and blue curves represent the lower and upper limits of $(L/R)_c$ when β_i varies from 0 to 1, with $(L/R)_c = \pi/(k_c R)$ denoting the critical length-to-half-width-ratio. Trapped (leaky) modes lie on the right (left) of these lines, and hence $\delta\tau$ is undefined in the lower-right corner of Figure 6b. One sees that the red and blue curves differ little, which is not surprising given the insensitive dependence of $k_c R$ on β_i .

What is more interesting is that neither P nor τ is sensitive to β_i as long as they are measured in units of the transverse fast time R/v_{fi} . Figure 6b indicates that $\delta\tau$ exceeds 10% only in the immediate vicinity of the red or blue curve, as represented by the hatched portion. Regarding the periods, Figure 6a indicates that δP is consistently smaller than 1.2%. This β_i dependence is even weaker than for kink I (see Figure 4). However, it should be noted that in cold MHD the specific values of P and τ are rather sensitive to the parameters characterizing the TL, i.e., ρ_i/ρ_e and l/R . At a given pair of ρ_i/ρ_e and l/R , they are also considerably influenced by how the TL profile is prescribed (paper I). Therefore what Figure 6 indicates is that, if P and τ of kink II are to be used for seismological purposes, then one can use the much simpler cold MHD theory as presented in paper I. The difference between kink I and kink II is that, while one can use the even simpler theory for top-hat profiles to evaluate P for kink I, the details of the TL profiles have to be taken into account when P and τ are evaluated for kink II.

4.2.4. First Branch of Sausage Modes

The influence of β_i on sausage I can be examined in a manner identical to kink II. Figure 7 shows the critical wavenumber $k_c R$ as a function of β_i for parabolic profiles with a number of different combinations of ρ_i/ρ_e and l/R . Evidently, the behavior of $k_c R$ is qualitatively the same as for kink II. Once again, by far the most important factor that influences $k_c R$ is the density contrast, and the role played by β_i is marginal to say the most. Similar to kink II, this insensitive dependence on β_i can be partly understood from Equation (34) pertinent to top-hat profiles. The only difference is that g_2 needs to be replaced with $\pi/2$ (see Eq. 27). Note that for top-hat profiles, this weak dependence of $k_c R$ on β_i was already shown for sausage modes by Inglis et al. (2009). What Figure 7 shows is that this weak dependence

persists for continuous profiles as well.

The β_i dependence of the periods P and damping times τ is brought out also by examining how they differ from the cold MHD results. Similar to Figure 6, now δP and $\delta\tau$ are presented in Figure 8 as functions of ρ_i/ρ_e and L/R . Comparing Figure 8b with Figure 6b indicates that the hatched portion where $\delta\tau$ exceeds 10% is somehow broader than for kink II. Nonetheless, in the majority of the parameter space, the influence of β_i on τ tends to be marginal to say the most. This weak β_i dependence is even more pronounced for the periods, for which Figure 8a indicates that P differs from its cold MHD counterpart by no more than 3%. Now recall that our paper I has demonstrated that in cold MHD, the periods and damping times for sausage I are sensitive to the profile prescriptions. Therefore our conclusion regarding sausage I is identical to kink II, namely the corresponding P and τ can be evaluated with the DR in cold MHD (Equation 17 in paper I) by properly accounting for the transverse density distribution. The effect of a finite β_i is secondary, as long as P and τ are measured in units of the transverse fast time.

5. SUMMARY AND CONCLUDING REMARKS

This study has been motivated by the apparent lack of a theoretical examination on the combined effects on fast standing modes of a finite plasma beta inside and a continuous distribution of equilibrium parameters across solar coronal slabs. In the framework of ideal MHD with finite gas pressure, we worked out a rather generic dispersion relation (Equation 22) governing fast modes in magnetic slabs for which the transverse profiles comprise a uniform core, a uniform external medium, and a transition layer (TL) sandwiched in between. The profiles in the TL are allowed to be rather arbitrary. We have restricted our attention to the first several branches of fast modes, which are of observational interest in most cases. The influence of a finite plasma beta on the dispersive properties of these modes is brought out by examining how the periods (P), damping times (τ), and critical longitudinal wavenumbers (k_c) are affected. Our numerical results indicated that for parameters typical of coronal structures, the influence due to a finite plasma beta is at most marginal, as long as both P and τ are measured in units of the transverse fast time. Putting these results together with our cold MHD results as presented in Yu et al. (2015), we conclude that for the first branch of sausage modes and second branch of kink modes alike, P and τ can be evaluated with the theoretical results found for cold slabs provided that the transverse profiles are properly accounted for and the transverse Alfvén time in cold MHD is replaced with the transverse fast time. For the first branch of kink modes, one can use the even simpler theory for cold slabs with top-hat density profiles because their periods are not sensitive to either the layer

width or how the density profile is prescribed in the TL.

This study can be extended in a number of ways. For instance, by accounting for the out-of-plane propagation, the interesting physics of resonant coupling of fast kink waves to the Alfvén continuum can be examined (e.g., [Arregui et al. 2007b](#)). In this case, a singular series expansion, rather than the regular series expansion that was adopted here, is necessary to solve the governing differential equation (see [Soler et al. 2013](#) for the application of this approach in the cylindrical geometry). When this approach is implemented, the resonant coupling of slow modes to the cusp continuum can also be addressed, and the finite gas pressure is expected to play an important role. Furthermore, by allowing the physical parameters in the environment to be asymmetric about the slab axis, one will be able to examine how a continuous transverse profile affects the waves modes, which can no longer be strictly classified into kink and sausage modes ([Allcock & Erdélyi 2017](#)). This is expected to find applications to structures in the lower solar atmosphere, those close to the magnetic canopy for instance.

We thank the referee for his/her constructive comments. This work is supported by the National Natural Science Foundation of China (BL:41674172, 11761141002, and 41474149, SXC:41604145, HY:41704165), and by the Provincial Natural Science Foundation of Shandong via Grants JQ201212 (BL) and ZR2016DP03 (HY).

REFERENCES

- Allcock, M. & Erdélyi, R. 2017, *Sol. Phys.*, 292, 35
- Arregui, I., Andries, J., Van Doorselaere, T., Goossens, M., & Poedts, S. 2007a, *A&A*, 463, 333
- Arregui, I. & Asensio Ramos, A. 2014, *A&A*, 565, A78
- Arregui, I., Oliver, R., & Ballester, J. L. 2012, *Living Reviews in Solar Physics*, 9, 2
- Arregui, I., Soler, R., & Asensio Ramos, A. 2015, *ApJ*, 811, 104
- Arregui, I., Terradas, J., Oliver, R., & Ballester, J. L. 2007b, *Sol. Phys.*, 246, 213
- Aschwanden, M. J., Fletcher, L., Schrijver, C. J., & Alexander, D. 1999, *ApJ*, 520, 880
- Aschwanden, M. J., Nakariakov, V. M., & Melnikov, V. F. 2004, *ApJ*, 600, 458
- Aschwanden, M. J. & Schrijver, C. J. 2011, *ApJ*, 736, 102

- Banerjee, D., Erdélyi, R., Oliver, R., & O’Shea, E. 2007, *Sol. Phys.*, 246, 3
- Cally, P. S. 1986, *Sol. Phys.*, 103, 277
- Chen, S.-X., Li, B., Xia, L.-D., Chen, Y.-J., & Yu, H. 2014, *Sol. Phys.*, 289, 1663
- Chen, S.-X., Li, B., Xiong, M., Yu, H., & Guo, M.-Z. 2016, *ApJ*, 833, 114 (paper II)
- Chen, Y., Feng, S. W., Li, B., Song, H. Q., Xia, L. D., Kong, X. L., & Li, X. 2011, *ApJ*, 728, 147
- Chen, Y., Song, H. Q., Li, B., Xia, L. D., Wu, Z., Fu, H., & Li, X. 2010, *ApJ*, 714, 644
- De Moortel, I. & Nakariakov, V. M. 2012, *Philosophical Transactions of the Royal Society of London Series A*, 370, 3193
- Dennis, B. R., Tolbert, A. K., Inglis, A., Ireland, J., Wang, T., Holman, G. D., Hayes, L. A., & Gallagher, P. T. 2017, *ApJ*, 836, 84
- Dorotovič, I., Erdélyi, R., Freij, N., Karlovský, V., & Márquez, I. 2014, *A&A*, 563, A12
- Dorotovič, I., Erdélyi, R., & Karlovský, V. 2008, in *IAU Symposium, Vol. 247, Waves & Oscillations in the Solar Atmosphere: Heating and Magneto-Seismology*, ed. R. Erdélyi & C. A. Mendoza-Briceno, 351–354
- Edwin, P. M. & Roberts, B. 1982, *Sol. Phys.*, 76, 239
- . 1983, *Sol. Phys.*, 88, 179
- . 1988, *A&A*, 192, 343
- Edwin, P. M., Roberts, B., & Hughes, W. J. 1986, *Geophys. Res. Lett.*, 13, 373
- Erdélyi, R. & Taroyan, Y. 2008, *A&A*, 489, L49
- Feng, S. W., Chen, Y., Li, B., Song, H. Q., Kong, X. L., Xia, L. D., & Feng, X. S. 2011, *Sol. Phys.*, 272, 119
- Freij, N., Dorotovič, I., Morton, R. J., Ruderman, M. S., Karlovský, V., & Erdélyi, R. 2016, *ApJ*, 817, 44
- Goossens, M., Arregui, I., Ballester, J. L., & Wang, T. J. 2008, *A&A*, 484, 851
- Grant, S. D. T., Jess, D. B., Moreels, M. G., Morton, R. J., Christian, D. J., Giagkiozis, I., Verth, G., Fedun, V., Keys, P. H., Van Doorselaere, T., & Erdélyi, R. 2015, *ApJ*, 806, 132

- Guo, M.-Z., Chen, S.-X., Li, B., Xia, L.-D., & Yu, H. 2016, *Sol. Phys.*, 291, 877
- Hornsey, C., Nakariakov, V. M., & Fludra, A. 2014, *A&A*, 567, A24
- Huang, P., Musielak, Z. E., & Ulmschneider, P. 1999, *A&A*, 342, 300
- Inglis, A. R., van Doorselaere, T., Brady, C. S., & Nakariakov, V. M. 2009, *A&A*, 503, 569
- Jafarzadeh, S., Solanki, S. K., Gafeira, R., van Noort, M., Barthol, P., Blanco Rodríguez, J., del Toro Iniesta, J. C., Gandorfer, A., Gizon, L., Hirzberger, J., Knölker, M., Orozco Suárez, D., Riethmüller, T. L., & Schmidt, W. 2017, *ApJS*, 229, 9
- Jelínek, P. & Karlický, M. 2012, *A&A*, 537, A46
- Jelínek, P., Karlický, M., & Murawski, K. 2012, *A&A*, 546, A49
- Karlický, M., Mészárosóvá, H., & Jelínek, P. 2013, *A&A*, 550, A1
- Kuridze, D., Verth, G., Mathioudakis, M., Erdélyi, R., Jess, D. B., Morton, R. J., Christian, D. J., & Keenan, F. P. 2013, *ApJ*, 779, 82
- Li, B., Habbal, S. R., & Chen, Y. 2013, *ApJ*, 767, 169
- Lopin, I. & Nagorny, I. 2015, *ApJ*, 801, 23
- Macnamara, C. K. & Roberts, B. 2011, *A&A*, 526, A75
- Melnikov, V. F., Reznikova, V. E., Shibasaki, K., & Nakariakov, V. M. 2005, *A&A*, 439, 727
- Mészárosóvá, H., Karlický, M., Jelínek, P., & Rybák, J. 2014, *ApJ*, 788, 44
- Mignone, A., Bodo, G., Massaglia, S., Matsakos, T., Tesileanu, O., Zanni, C., & Ferrari, A. 2007, *ApJS*, 170, 228
- Mooroogen, K., Morton, R. J., & Henriques, V. 2017, *ArXiv e-prints*, 1708.03500
- Morton, R. J., Erdélyi, R., Jess, D. B., & Mathioudakis, M. 2011, *ApJ*, 729, L18
- Morton, R. J., Verth, G., Jess, D. B., Kuridze, D., Ruderman, M. S., Mathioudakis, M., & Erdélyi, R. 2012, *Nature Communications*, 3, 1315
- Murawski, K. & Roberts, B. 1993, *Sol. Phys.*, 143, 89
- Nakariakov, V. M. & Melnikov, V. F. 2009, *Space Sci. Rev.*, 149, 119

- Nakariakov, V. M., Ofman, L., Deluca, E. E., Roberts, B., & Davila, J. M. 1999, *Science*, 285, 862
- Nakariakov, V. M., Pilipenko, V., Heilig, B., Jelínek, P., Karlický, M., Klimushkin, D. Y., Kolotkov, D. Y., Lee, D.-H., Nisticò, G., Van Doorselaere, T., Verth, G., & Zimovets, I. V. 2016, *Space Sci. Rev.*, 200, 75
- Nakariakov, V. M. & Roberts, B. 1995a, *Sol. Phys.*, 159, 213
- . 1995b, *Sol. Phys.*, 159, 399
- Nakariakov, V. M. & Verwichte, E. 2005, *Living Reviews in Solar Physics*, 2, 3
- Ofman, L., Davila, J. M., & Steinolfson, R. S. 1994, *ApJ*, 421, 360
- Ofman, L. & Wang, T. J. 2008, *A&A*, 482, L9
- Pascoe, D. J., Goddard, C. R., Anfinogentov, S., & Nakariakov, V. M. 2017, *A&A*, 600, L7
- Porter, L. J., Klimchuk, J. A., & Sturrock, P. A. 1994, *ApJ*, 435, 502
- Roberts, B. 2000, *Sol. Phys.*, 193, 139
- Roberts, B. 2008, in *IAU Symposium, Vol. 247, Waves & Oscillations in the Solar Atmosphere: Heating and Magneto-Seismology*, ed. R. Erdélyi & C. A. Mendoza-Briceno, 3–19
- Rosenberg, H. 1970, *A&A*, 9, 159
- Smith, J. M., Roberts, B., & Oliver, R. 1997, *A&A*, 327, 377
- Soler, R., Goossens, M., Terradas, J., & Oliver, R. 2013, *ApJ*, 777, 158
- . 2014, *ApJ*, 781, 111
- Spruit, H. C. 1982, *Sol. Phys.*, 75, 3
- Su, J. T., Shen, Y. D., Liu, Y., Liu, Y., & Mao, X. J. 2012, *ApJ*, 755, 113
- Terradas, J., Andries, J., & Goossens, M. 2007, *Sol. Phys.*, 246, 231
- Terradas, J., Oliver, R., & Ballester, J. L. 2005, *A&A*, 441, 371
- Tian, H., Young, P. R., Reeves, K. K., Wang, T., Antolin, P., Chen, B., & He, J. 2016, *ApJ*, 823, L16

- Van Doorselaere, T., Kupriyanova, E. G., & Yuan, D. 2016, *Sol. Phys.*, 291, 3143
- Verwichte, E., Aschwanden, M. J., Van Doorselaere, T., Foullon, C., & Nakariakov, V. M. 2009, *ApJ*, 698, 397
- Verwichte, E., Nakariakov, V. M., & Cooper, F. C. 2005, *A&A*, 430, L65
- Wang, T., Innes, D. E., & Qiu, J. 2007, *ApJ*, 656, 598
- Wang, T. J. 2016, Washington DC American Geophysical Union Geophysical Monograph Series, 216, 395
- Yu, H., Li, B., Chen, S.-X., & Guo, M.-Z. 2015, *ApJ*, 814, 60 (paper I)
- Yu, H., Li, B., Chen, S.-X., Xiong, M., & Guo, M.-Z. 2016a, *ApJ*, 833, 51
- . 2017, *ApJ*, 836, 1
- Yu, S., Nakariakov, V. M., & Yan, Y. 2016b, *ApJ*, 826, 78
- Zajtsev, V. V. & Stepanov, A. V. 1975, *Issledovaniia Geomagnetizmu Aeronomii i Fizike Solntsa*, 37, 3

APPENDIX

A. Coefficients in the expressions for $\tilde{\xi}_{\text{tr},1}(\epsilon)$ and $\tilde{\xi}_{\text{tr},2}(\epsilon)$

A.1. Coefficients for general profiles in the transition layer

For general density and temperature profiles in the transition layer described in Equations (7) and (8), the coefficients a_n and b_n in $\tilde{\xi}_{\text{tr},1}(\epsilon) = \sum_{n=0}^{\infty} a_n \epsilon^n$ and $\tilde{\xi}_{\text{tr},2}(\epsilon) = \sum_{n=0}^{\infty} b_n \epsilon^n$ are given by

$$\left\{ \begin{array}{l} a_0 = R \\ a_1 = 0 \end{array} \right. \quad \text{and} \quad \left\{ \begin{array}{l} b_0 = 0 \\ b_1 = 1 \end{array} \right. . \quad (\text{A1})$$

From this point onward, let χ denote either a or b , since both obey the same recurrence relations. The coefficients χ_i for $i \geq 2$ are then given by

$$\chi_i = -\frac{D(k, \omega^2)}{i(i-1)C(k, \omega^2)} \quad (\text{A2})$$

where

$$\begin{aligned} C(k, \omega^2) = & 2\omega^4 C_0^2 + \gamma\omega^4 C_0 V_0 - 2k^2\omega^2 C_0^3 - \gamma k^2\omega^2 C_0^2 V_0 + 2\omega^4 C_0 V_0 + \gamma\omega^4 V_0^2 \\ & - 4k^2\omega^2 C_0^2 V_0 - 2\gamma k^2\omega^2 V_0^2 C_0 + 2k^4 C_0^3 V_0 + \gamma k^4 C_0^2 V_0^2 \end{aligned} \quad (\text{A3})$$

and

$$D(k, \omega^2) = D_1(k, \omega^2) + D_2(k, \omega^2) + D_3(k, \omega^2)$$

$$\begin{aligned} & D_1(k, \omega^2) \\ = & \omega^4 \sum_{m=0}^{i-3} \sum_{j=0}^{i-2-m} (m+2)(m+1) (C_{i-2-j-m} + V_{i-2-j-m}) (2C_j + \gamma V_j) \chi_{m+2} \\ & - k^2\omega^2 \sum_{m=0}^{i-3} \sum_{j=0}^{i-2-m} \sum_{l=0}^{i-2-j-m} (m+2)(m+1) (C_{i-2-l-j-m} + 2V_{i-2-l-j-m}) (2C_j + \gamma V_j) C_l \chi_{m+2} \\ & + k^4 \sum_{m=0}^{i-3} \sum_{j=0}^{i-2-m} \sum_{l=0}^{i-2-j-m} \sum_{s=0}^{i-2-j-l-m} (m+2)(m+1) C_{i-2-j-l-m-s} V_s C_j (2C_l + \gamma V_l) \chi_{m+2} \end{aligned} \quad (\text{A4})$$

$$\begin{aligned} & D_2(k, \omega^2) \\ = & \omega^4 \sum_{m=0}^{i-2} \sum_{j=0}^{i-2-m} (j+1)(2-\gamma) (C_{i-2-j-m} V_{j+1} - C_{j+1} V_{i-2-j-m}) (m+1) \chi_{m+1} \\ & + k^2\omega^2 \sum_{m=0}^{i-2} \sum_{j=0}^{i-2-m} \sum_{l=0}^{i-2-j-m} (m+1)(j+1) (4V_l C_{j+1} + \gamma C_l V_{j+1} + 2C_l C_{j+1} - 4C_l V_{j+1}) C_{i-2-j-l-m} \chi_{m+1} \\ & + 2k^4 \sum_{m=0}^{i-2} \sum_{j=0}^{i-2-m} \sum_{l=0}^{i-2-j-m} \sum_{s=0}^{i-2-j-l-m} (j+1) (C_s V_{j+1} - V_s C_{j+1}) C_{i-2-j-l-m-s} C_l (m+1) \chi_{m+1} \end{aligned} \quad (\text{A5})$$

$$\begin{aligned} & D_3(k, \omega^2) \\ = & \omega^6 \sum_{m=0}^{i-2} (2C_{i-2-m} + \gamma V_{i-2-m}) \chi_m - k^2\omega^4 \sum_{m=0}^{i-2} \sum_{j=0}^{i-2-m} (2C_j + \gamma V_j) (2C_{i-2-j-m} + V_{i-2-j-m}) \chi_m \\ & + k^4\omega^2 \sum_{m=0}^{i-2} \sum_{j=0}^{i-2-m} \sum_{l=0}^{i-2-j-m} C_{i-2-j-l-m} (2C_j + \gamma V_j) (C_l + 2V_l) \chi_m \\ & - k^6 \sum_{m=0}^{i-2} \sum_{j=0}^{i-2-m} \sum_{l=0}^{i-2-j-m} \sum_{s=0}^{i-2-j-l-m} C_{i-2-j-l-m-s} C_s (2C_j + \gamma V_j) V_l \chi_m. \end{aligned} \quad (\text{A6})$$

A.2. Simplified Coefficients for Profiles Specified in Equation (29)

Given that the coefficients C_i ($i > 2$) are all zero for the equilibrium profiles given by Equation (29), we can avoid the most time-consuming part when evaluating the coefficients a_i and b_i by simplifying the 4-fold summations. For $i \geq 6$, the terms D_1 , D_2 and D_3 in Equation (A2) can be reformulated such that only 2-fold summations are involved. In other words,

$$\begin{aligned}
 D_1(k, \omega^2) = & \sum_{m=0}^{i-3} \sum_{j=0}^{i-2-m} (m+2)(m+1)\chi_{m+2}(2C_j + \gamma V_j) \left[\omega^4(C_{i-2-j-m} + V_{i-2-j-m}) \right. \\
 & \left. - k^2\omega^2 C_0(C_{i-2-j-m} + 2V_{i-2-j-m}) + k^4 C_0^2 V_{i-2-j-m} \right] \\
 & + \sum_{m=0}^{i-3} \sum_{j=0}^{i-3-m} (m+2)(m+1)(2C_j + \gamma V_j)\chi_{m+2} \\
 & \left[2k^4 C_0 C_1 V_{i-3-j-m} - k^2\omega^2 C_1(C_{i-3-j-m} + 2V_{i-3-j-m}) \right] \\
 & + \sum_{m=0}^{i-4} \sum_{j=0}^{i-4-m} (m+2)(m+1)(2C_j + \gamma V_j)\chi_{m+2} \\
 & \left[k^4(C_1^2 + 2C_0 C_2)V_{i-4-j-m} - k^2\omega^2 C_2(C_{i-4-j-m} + 2V_{i-4-j-m}) \right] \\
 & + 2k^4 C_1 C_2 \sum_{m=0}^{i-5} \sum_{j=0}^{i-5-m} V_{i-5-j-m} (m+2)(m+1)(2C_j + \gamma V_j)\chi_{m+2} \\
 & + k^4 C_2^2 \sum_{m=0}^{i-6} \sum_{j=0}^{i-6-m} V_{i-6-j-m} (m+2)(m+1)(2C_j + \gamma V_j)\chi_{m+2},
 \end{aligned} \tag{A7}$$

$$\begin{aligned}
& D_2(k, \omega^2) \\
&= \sum_{m=0}^{i-2} \sum_{j=0}^{i-2-m} (j+1)(m+1)\chi_{m+1} [\omega^4(2-\gamma)(C_{i-2-j-m}V_{j+1} - C_{j+1}V_{i-2-j-m}) \\
&\quad + k^2\omega^2C_0(4V_{i-2-j-m}C_{j+1} + \gamma C_{i-2-j-m}V_{j+1} + 2C_{i-2-j-m}C_{j+1} - 4C_{i-2-j-m}V_{j+1}) \\
&\quad + 2k^4C_0^2(C_{i-2-j-m}V_{j+1} - V_{i-2-j-m}C_{j+1})] \\
&+ \sum_{m=0}^{i-3} \sum_{j=0}^{i-3-m} (j+1)(m+1)\chi_{m+1} [4k^4C_0C_1(C_{i-3-j-m}V_{j+1} - V_{i-3-j-m}C_{j+1}) \\
&\quad + k^2\omega^2C_1(4V_{i-3-j-m}C_{j+1} + \gamma C_{i-3-j-m}V_{j+1} + 2C_{i-3-j-m}C_{j+1} - 4C_{i-3-j-m}V_{j+1})] \\
&+ \sum_{m=0}^{i-4} \sum_{j=0}^{i-4-m} (j+1)(m+1)\chi_{m+1} [2k^4(C_1^2 + 2C_0C_2)(C_{i-4-j-m}V_{j+1} - V_{i-4-j-m}C_{j+1}) \\
&\quad + k^2\omega^2C_2(4V_{i-4-j-m}C_{j+1} + \gamma C_{i-4-j-m}V_{j+1} + 2C_{i-4-j-m}C_{j+1} - 4C_{i-4-j-m}V_{j+1})] \\
&+ 4k^4C_1C_2 \sum_{m=0}^{i-5} \sum_{j=0}^{i-5-m} (j+1)(m+1)\chi_{m+1}(C_{i-5-j-m}V_{j+1} - V_{i-5-j-m}C_{j+1}) \\
&+ 2k^4C_2^2 \sum_{m=0}^{i-6} \sum_{j=0}^{i-6-m} (j+1)(m+1)\chi_{m+1}(C_{i-6-j-m}V_{j+1} - V_{i-6-j-m}C_{j+1}),
\end{aligned} \tag{A8}$$

and

$$\begin{aligned}
D_3(k, \omega^2) &= \omega^6 \sum_{m=0}^{i-2} (2C_{i-2-m} + \gamma V_{i-2-m}) \chi_m \\
&+ \sum_{m=0}^{i-2} \sum_{j=0}^{i-2-m} \chi_m \left[-k^2 \omega^4 (2C_j + \gamma V_j) (2C_{i-2-j-m} + V_{i-2-j-m}) \right. \\
&\quad \left. + k^4 \omega^2 C_0 (2C_j + \gamma V_j) (C_{i-2-j-m} + 2V_{i-2-j-m}) \right. \\
&\quad \left. - k^6 C_0^2 (2C_j + \gamma V_j) V_{i-2-j-m} \right] \\
&+ \sum_{m=0}^{i-3} \sum_{j=0}^{i-3-m} \chi_m \left[k^4 \omega^2 C_1 (2C_j + \gamma V_j) (C_{i-3-j-m} + 2V_{i-3-j-m}) \right. \\
&\quad \left. - 2k^6 C_0 C_1 (2C_j + \gamma V_j) V_{i-3-j-m} \right] \\
&+ \sum_{m=0}^{i-4} \sum_{j=0}^{i-4-m} \chi_m \left\{ k^4 \omega^2 C_2 (2C_j + \gamma V_j) (C_{i-4-j-m} + 2V_{i-4-j-m}) \right. \\
&\quad \left. - k^6 (C_1^2 + 2C_0 C_2) (2C_j + \gamma V_j) V_{i-4-j-m} \right\} \\
&- 2k^6 C_1 C_2 \sum_{m=0}^{i-5} \sum_{j=0}^{i-5-m} (2C_j + \gamma V_j) V_{i-5-j-m} \chi_m \\
&- k^6 C_2^2 \sum_{m=0}^{i-6} \sum_{j=0}^{i-6-m} (2C_j + \gamma V_j) V_{i-6-j-m} \chi_m.
\end{aligned} \tag{A9}$$

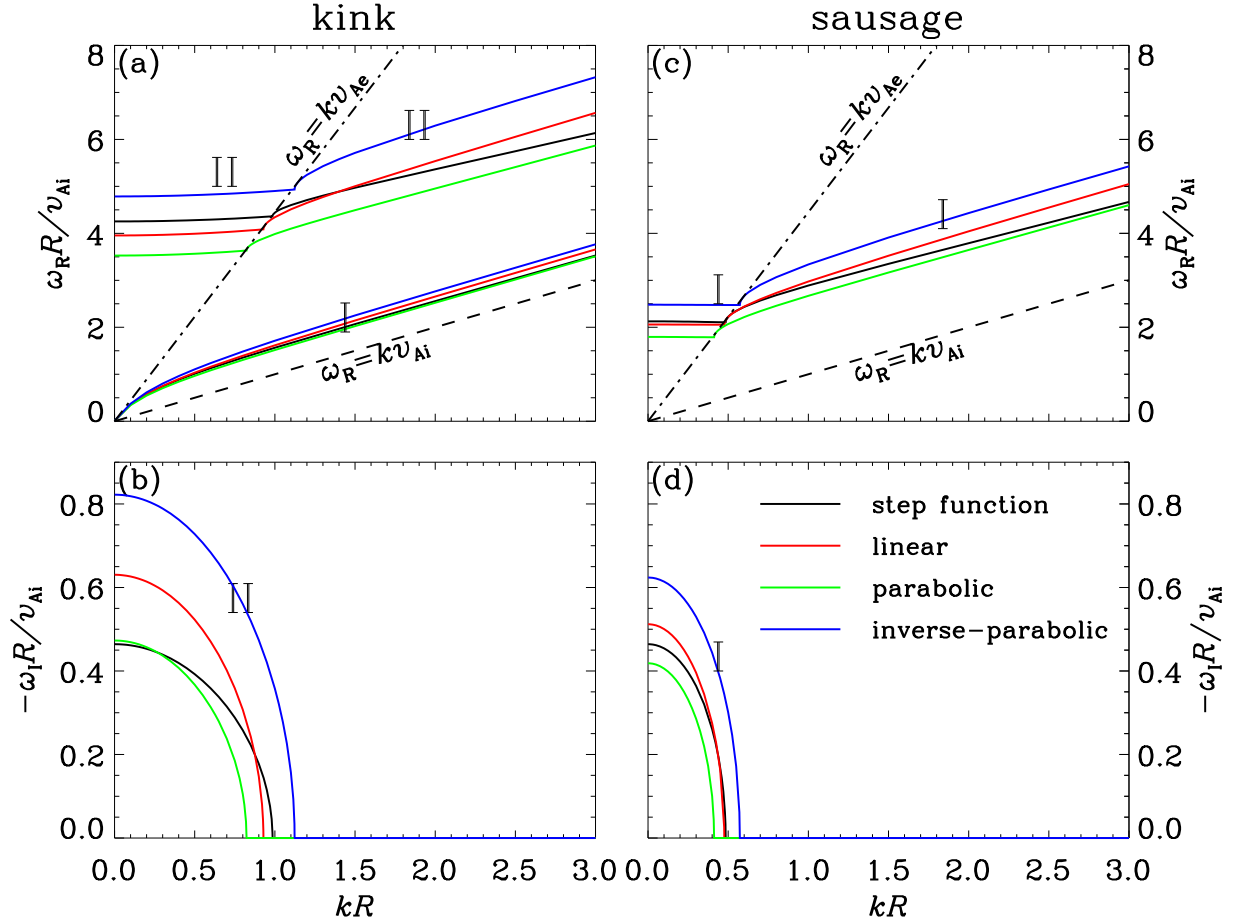


Fig. 1.— Illustration of profile prescriptions using transverse equilibrium density profiles as an example. These profiles differ only in a transition layer sandwiched between the internal (with a uniform density ρ_i) and external (with a uniform density ρ_e) portions. This transition layer is of width l and is located between $x_i = R - l/2$ and $x_e = R + l/2$, with R being the mean half-width. Three different profile prescriptions are adopted as labeled and are given by Equation (29). For illustration purposes, $l = R$ and $\rho_i/\rho_e = 50$.

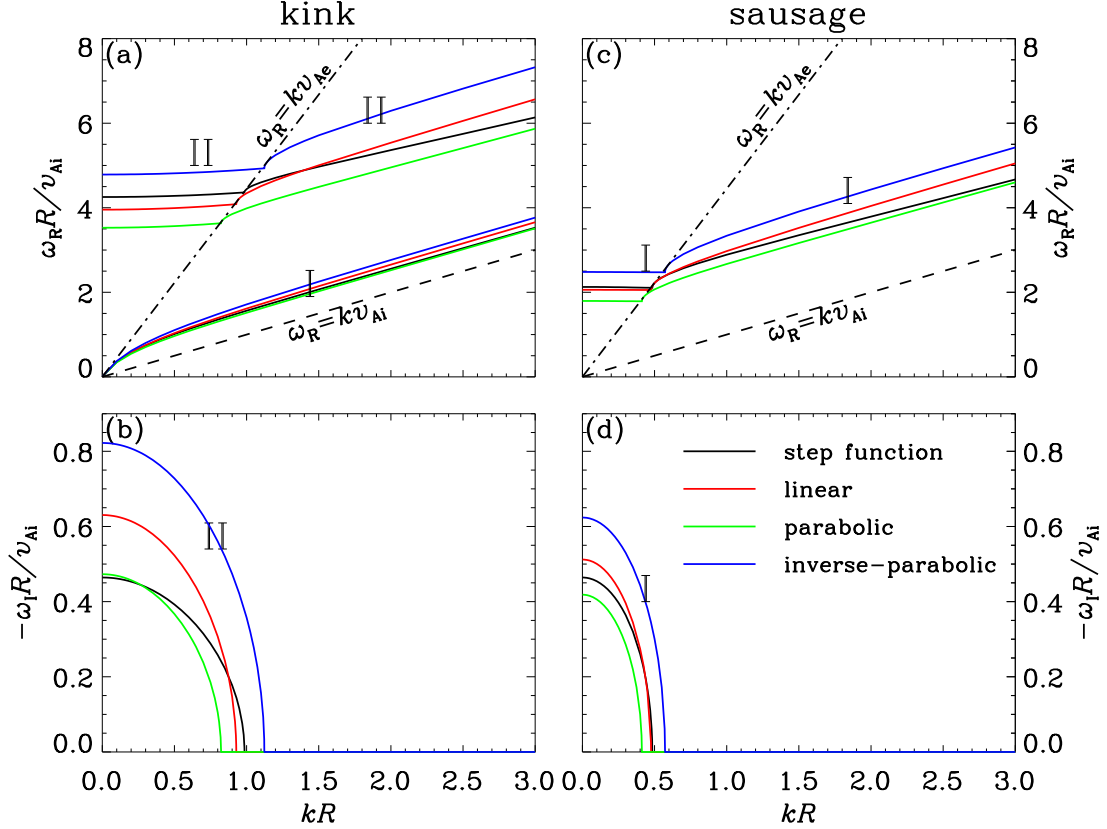


Fig. 2.— Dispersion diagrams for fast kink (left) and sausage (right) modes in nonuniform coronal slabs with a finite beta. The real (ω_R , the upper row) and imaginary (ω_I , lower row) parts of the angular frequency are shown as functions of the real-valued longitudinal wavenumber k . These solutions are found by solving the dispersion relation (Equation (22)) for three different profiles, represented by the curves in different colors. The corresponding result for a step-function profile is given by the black solid curves for comparison. In (a) and (c), the black dash-dotted (dashed) lines represent $\omega_R = kv_{Ae}$ ($\omega_R = kv_{Ai}$). The former separates the trapped (to its right) from leaky (left) regimes, and the latter is the lower limit of ω_R in coronal slabs. Here the width of the transition layer $l = R$, the density contrast $\rho_i/\rho_e = 10$ and the internal beta $\beta_i = 1$. The external plasma beta is fixed at 0.01.

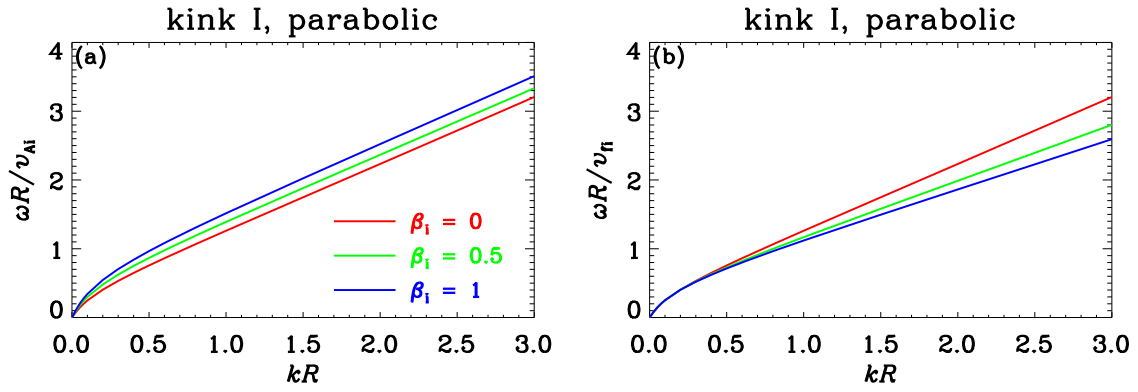


Fig. 3.— Dispersion diagrams for the first branch of standing kink modes in nonuniform coronal slabs with a finite beta. The angular frequency ω in units of v_{Ai}/R (panel a) and v_{fi}/R (panel b) are shown as functions of the longitudinal wavenumber k . The red, green, and blue curves correspond to $\beta_i = 0, 0.5,$ and 1 , respectively. Here the transverse profile is parabolic, the width of the transition layer is $l = R$, and the density contrast is $\rho_i/\rho_e = 10$.

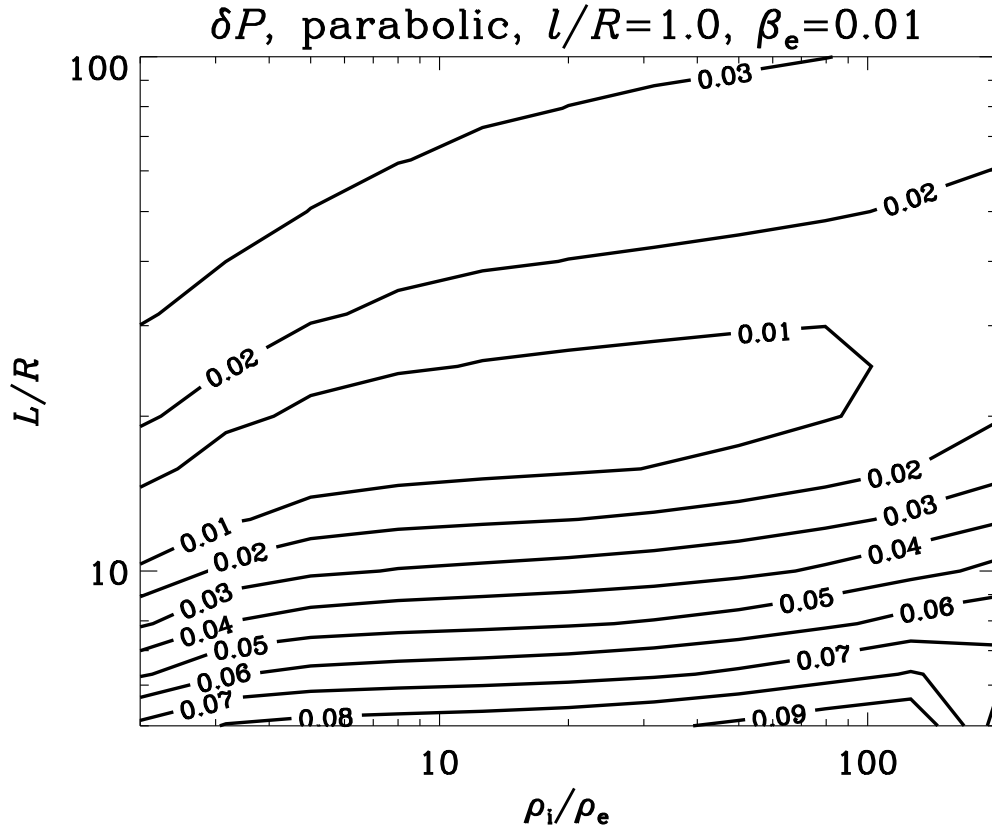


Fig. 4.— Distributions of δP for the first branch of kink modes in the space spanned by ρ_i/ρ_e and L/R for parabolic profiles with $l/R = 1$. Here δP evaluates the maximal difference of the period P relative to the cold MHD result at a given pair $[\rho_i/\rho_e, L/R]$ when β_i varies between 0 and 1. See text for details.

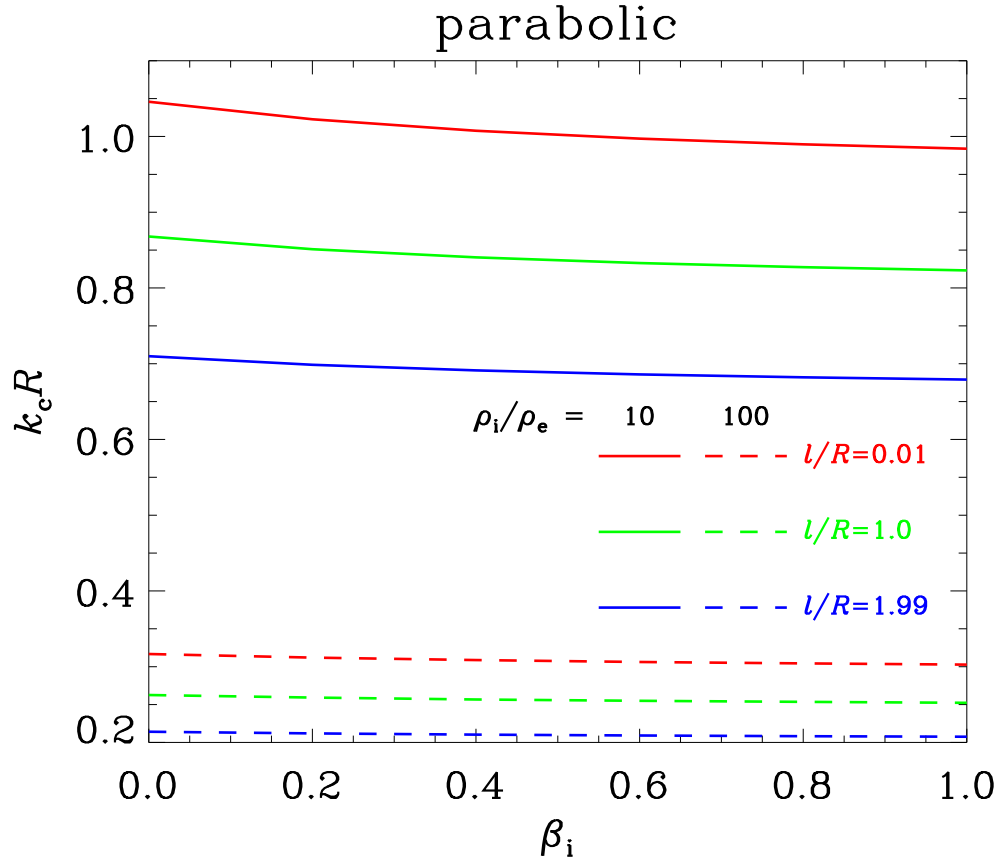


Fig. 5.— Dependence on the internal plasma beta (β_i) of critical wavenumbers k_c of the second branch of kink modes in transversely continuous slabs with parabolic profiles. A number of combinations for the density contrast ρ_i/ρ_e and dimensionless layer width l/R are examined as labeled.

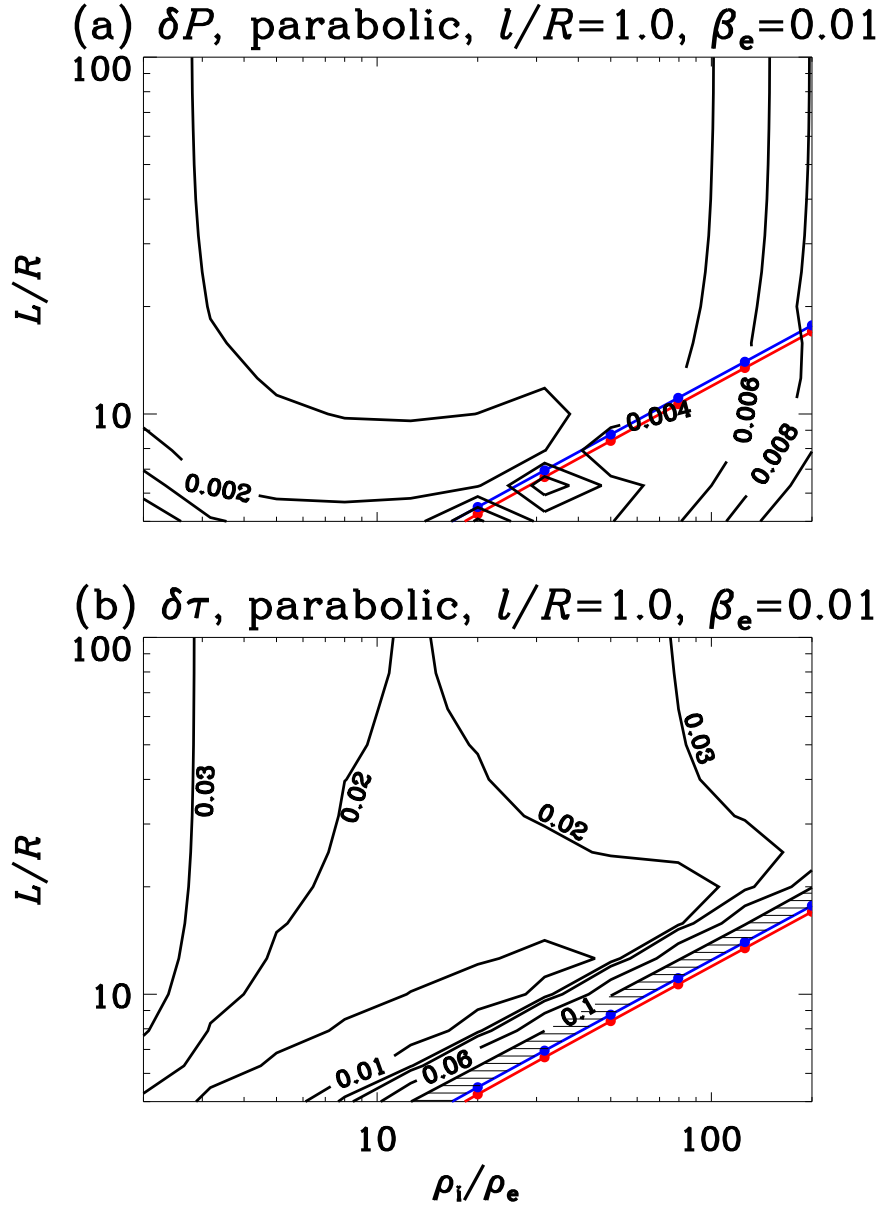


Fig. 6.— Distributions of δP and $\delta\tau$ for the second branch of kink modes in the space spanned by ρ_i/ρ_e and L/R for parabolic profiles with $l/R = 1$. Here δP ($\delta\tau$) evaluates the maximal difference of the period P (damping time τ) relative to the cold MHD result at a given pair $[\rho_i/\rho_e, L/R]$ when β_i varies between 0 and 1. In addition, the red and blue lines represent the lower and upper limits of the critical length-to-half-width-ratios at a given density contrast. The hatched area in panel (b) represents where $\delta\tau$ exceeds 10%. See text for details.

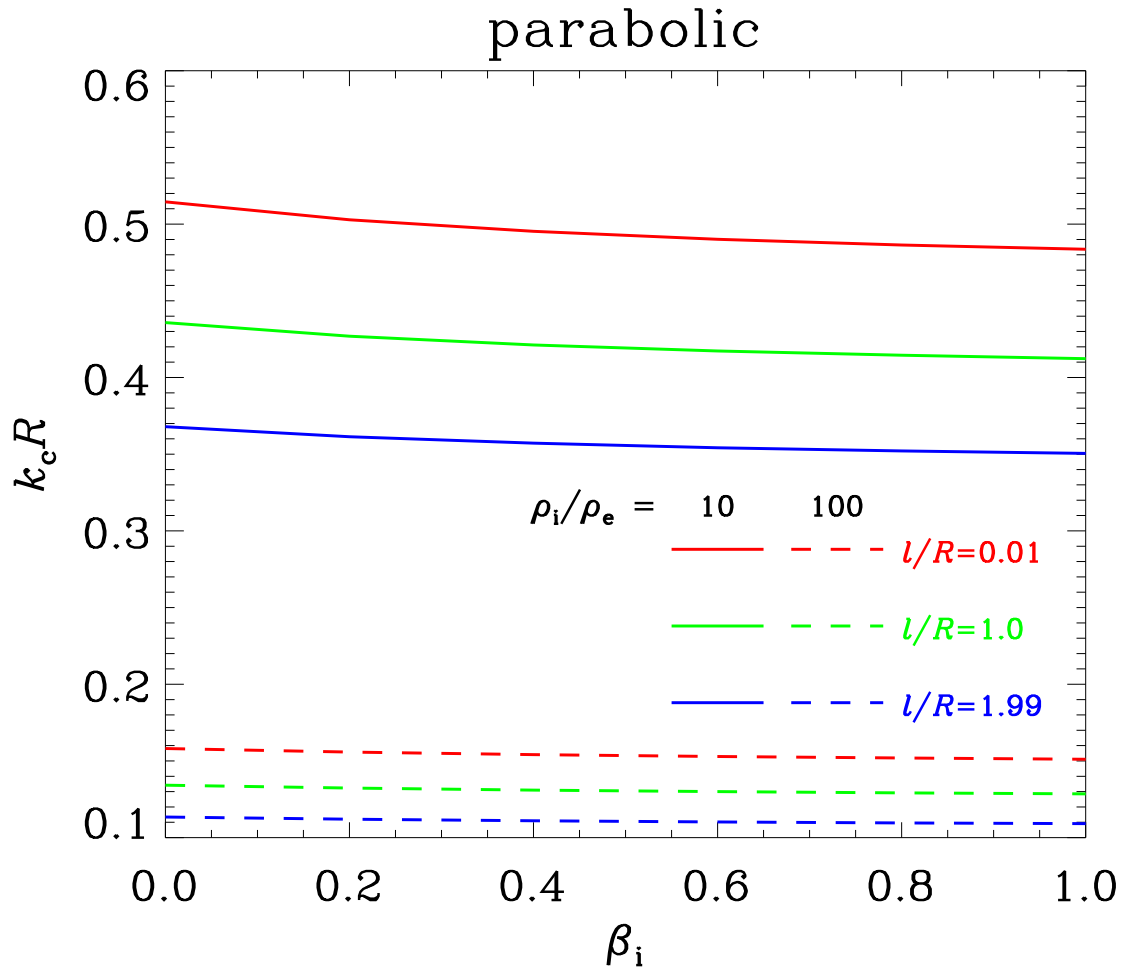


Fig. 7.— Similar to Figure 5 but for the first branch of sausage modes.

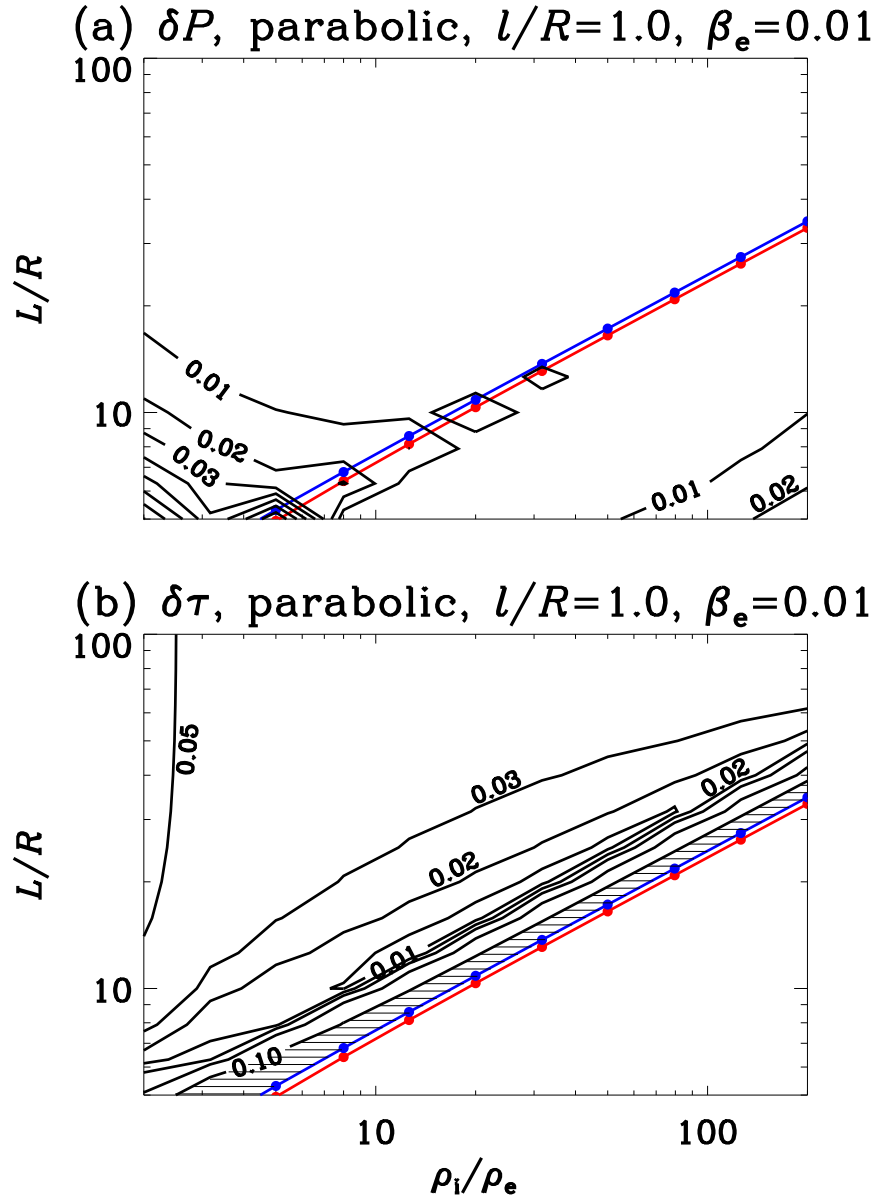


Fig. 8.— Similar to Figure 6 but for the first branch of sausage modes.